第 43 卷 第 22 期/2023 年 11 月/光学学报 研究论文

光学学报

高载流子迁移率胶体量子点红外探测器

薛晓梦[1]，马海菲[1,2]，郝群[1,2**]，唐鑫[1,2]，陈梦璐[1,2*]

[1]北京理工大学光电学院，北京 100081；

[2]北京理工大学长三角研究院，浙江 嘉兴 314019

摘要 采用混相配体交换的方法成功实现了载流子迁移率近2个量级的提升，达到1 $cm^2/(V\cdot s)$，同时还可以灵活调控N型、本征型和P型等掺杂类型。在此基础上，使用本征型碲化汞胶体量子点薄膜制备短波及中波红外光伏型探测器。截止波长为1.9 μm的短波红外探测器在300 K下的响应率为0.9 A/W，比探测率为4×10^{11} Jones；截止波长为4.2 μm的中波红外探测器在110 K下的响应率为1.1 A/W，比探测率为1.2×10^{11} Jones。在没有施加偏置电压的情况下，300 K下的短波红外光电探测器的外量子效率可以达到61%，110 K下的中波红外光电探测器的外量子效率可以达到30%。

关键词 探测器；量子点；高迁移率；光伏型红外光电探测器；配体交换

中图分类号 TH745 **文献标志码** A **DOI**：10.3788/AOS231215

1 引 言

红外探测技术在环境监测[1]、目标探测[2-4]、材料光谱分析[5]和自动驾驶[6-8]等领域有着广泛的应用。目前，红外探测器主要基于块体半导体材料，如碲镉汞(MCT)[9-10]、铟镓砷(InGaAs)[11]、Ⅱ类超晶格[12]等，这些材料大都采用外延生长方法制备，不仅价格高昂，而且需要复杂的倒装键合工艺才能与读出电路耦合，阻碍了红外探测器在应用领域的发展。胶体量子点(CQD)具有制备易、成本低、能带可调以及与硅电子工艺兼容等优势，为新型光电探测器的发展提供了良好条件[13]。过去的十多年里，基于红外胶体量子点的探测器取得了显著性进展[14]。以碲化汞胶体量子点红外探测器为例，目前已发展出光电导[15-17]、光电晶体管[18-19]、光伏型[20-25]、带内跃迁[26]、双波段[27]、红外焦平面[28-29]等类型的探测器，未来将有望与其他半导体材料相结合[30-31]，进一步拓宽量子点的应用领域。

目前，量子点红外光电探测器在比探测率、响应度等核心性能方面与传统块体半导体红外探测器仍存在一定差距[32]。通过调节掺杂浓度和迁移率可以实现对量子点输运性质的调控，这是提升量子点红外光电探测器性能的关键[26]。常见的提高量子点迁移率的方法是配体交换[33-35]。近年来，液相配体交换方法[36-37]实现了量子点的高迁移率[16]和可控掺杂[38-42]，已在多个量子点体系中证实了调控输运性质可以有效地提升光导型探测器的比探测率、响应率等核心性能[26]。

本文采用混相配体交换的方法将载流子迁移率提升至1 $cm^2/(V\cdot s)$，与之前的研究结果10^{-2} $cm^2/(V\cdot s)$[42]相比，实现了近2个量级的提升，并且实现了N型、本征型、P型等掺杂类型的调控。在此基础之上，进一步研究了输运性质对探测器性能的影响。与光导型探测器相比，光伏型探测器不需要额外施加偏置电压，没有散粒噪声，拥有更高的理论灵敏度。同时，使用高载流子迁移率的本征型碲化汞量子点薄膜制备了短波及中波红外光伏型光电探测器。其中，截止波长为1.9 μm的短波红外(SWIR)探测器在室温(300 K)下的响应率为0.9 A/W，比探测率为4×10^{11} Jones；截止波长为4.2 μm的中波红外(MWIR)探测器在110 K下的响应率为1.1 A/W，比探测率为1.2×10^{11} Jones。此外，在没有施加偏置电压的情况下，300 K下的短波红外光电探测器的外量子效率(EQE)可以达到61%，110 K下的中波红外光电探测器的外量子效率可以达到30%。

2 实验过程

2.1 材料的合成

2.1.1 碲前驱体的制备

在氮气环境下，称量1.276 g(1 mmol)碲颗粒装在玻璃瓶中，并加入10 mL的三正辛基膦(TOP)溶液，均匀搅拌至溶解，得到浅黄色的透明溶液，即TOPTe

收稿日期：2023-07-03；**修回日期**：2023-08-13；**录用日期**：2023-09-06；**网络首发日期**：2023-09-22

基金项目：国家自然科学基金(U22A2081，62105022)、中国科学技术协会青年托举工程(YESS20210142)、北京市科技新星计划(Z211100002121069)

通信作者：*menglu@bit.edu.cn；**qhao@bit.edu.cn

溶液。

2.1.2　碲化汞胶体量子点的合成

在氮气环境下，称量 0.1088 g(0.4 mmol，氮气环境下储存)氯化汞粉末置于玻璃瓶中，并加入 16 mL 油胺(OAM)溶液，均匀搅拌并加热至氯化汞粉末全部溶解。本实验合成短波红外和中波红外碲化汞胶体量子点的反应温度分别为 65 ℃和 95 ℃。使用移液枪取 0.4 mL 的 TOPTe 溶液，快速注入到溶于油胺的氯化汞溶液中，反应时间分别为 4 min 和 6 min。反应结束后加入 20 mL 无水四氯乙烯(TCE)作为淬火溶液。

2.1.3　碲化银纳米晶体颗粒的合成

在氮气环境下，称量 0.068 g(0.4 mmol)硝酸银，并加入 1 mL 油酸(OA)和 10 mL 油胺，均匀搅拌 30 min。溶解后，注入 1 mL TOP，快速加热至 160 ℃并持续 30～45 min。向反应溶液中注入 0.2 mL TOPTe (0.2 mmol)溶液，反应时间为 10 min。

2.2　碲化汞胶体量子点的混相配体交换

混相配体交换过程包括液相配体交换和固相配体交换。选择溴化双十二烷基二甲基铵(DDAB)作为催化剂，将碲化汞胶体量子点溶在正己烷溶液中，取 4 mL 混合溶液与 160 μL β-巯基乙醇(β-ME)和 8 mg DDAB 在 *N*, *N*-二甲基甲酰胺(DMF)中混合，由于正己烷和 DMF 的极性不同，溶液会出现分层现象，将上层的清澈正己烷溶液取出，保留溶解了量子点的 DMF 溶液，即完成液相配体交换。之后向溶液中加入异丙醇(IPA)进行离心，倒掉上清液，将沉淀物重新溶解在 60 μL DMF 中。固相配体交换是在制备量子点薄膜后，用 1,2-乙二硫醇(EDT)、盐酸(HCl)和 IPA(体积比为 1∶1∶20)混合溶液对已成膜的碲化汞胶体量子点表面进行处理。

2.3　碲化汞胶体量子点的掺杂调控

在调控碲化汞胶体量子点的掺杂方面，Hg^{2+}可以通过表面偶极子稳定量子点中的电子，因此本实验选择汞盐($HgCl_2$)来调控量子点的掺杂状态。在液相配体交换结束后，向溶于 DMF 的碲化汞胶体量子点溶液中加入 10 mg $HgCl_2$得到本征型碲化汞胶体量子点，加入 20 mg $HgCl_2$得到 N 型碲化汞胶体量子点。

2.4　材料表征

采用混相配体交换的方法不仅可以提高载流子迁移率，还可以通过表面偶极子调控碲化汞胶体量子点的掺杂密度。液相配体交换前后中波红外碲化汞胶体量子点的透射电子显微镜(TEM)图像如图 1(a)所示，可以看到，进行液相配体交换后的碲化汞胶体量子点的间距明显减小，排列更加紧密。致密的排列可以提高碲化汞胶体量子点对光的吸收率。混相配体交换后的短波红外和中波红外碲化汞胶体量子点的吸收光谱如图 1(b)所示。从图 1(b)可以看出，短波红外和中波红外碲化汞胶体量子点的吸收峰分别位于 5250 cm^{-1}和 2700 cm^{-1}。

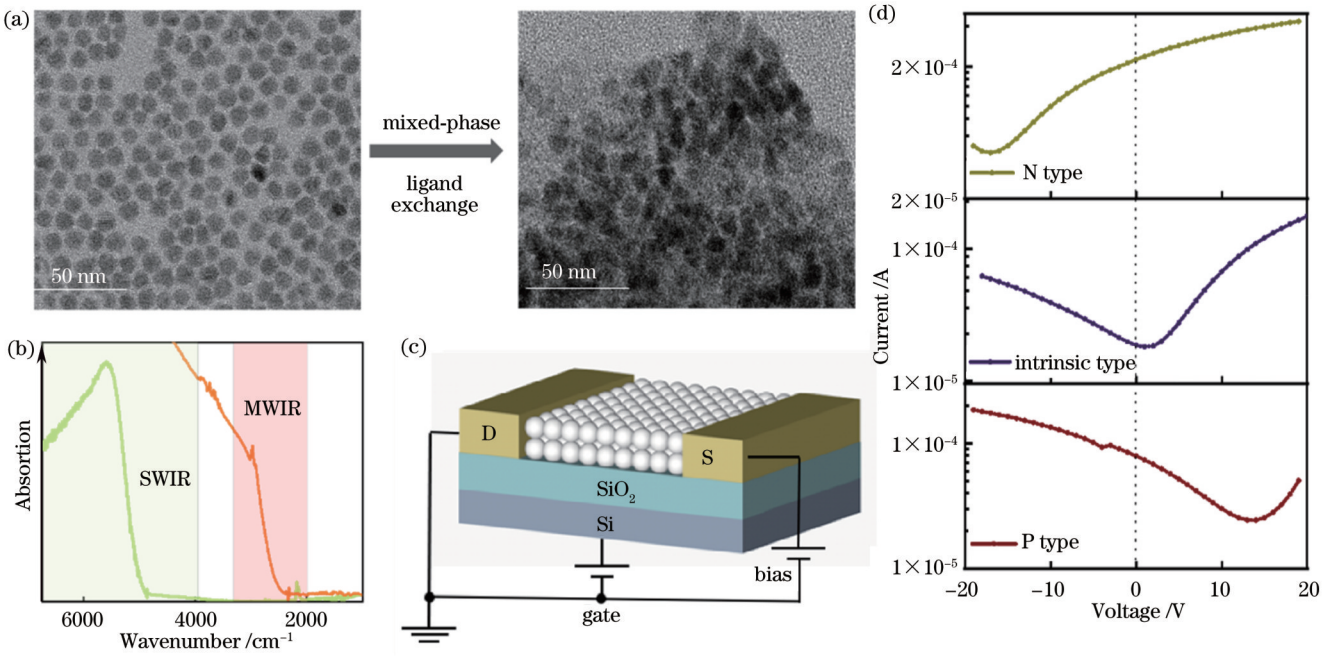

图 1　材料表征。(a)混相配体交换前后碲化汞胶体量子点的 TEM 图像；(b)短波红外和中波红外碲化汞胶体量子点的吸收光谱；(c) 碲化汞胶体量子点薄膜场效应晶体管测量原理图；(d)在 300 K 时，N 型、本征型和 P 型中波红外碲化汞胶体量子点的场效应晶体管转移曲线测试结果

Fig. 1　Material characterization. (a) TEM image of HgTe CQDs before and after mixed-phase ligand exchange; (b) absorption spectra of SWIR and MWIR; (c) schematic of FET measurement of HgTe CQDs film; (d) FET transfer curves of N type, intrinsic type, and P type MWIR HgTe CQDs at 300 K, respectively

利用场效应晶体管(FET)对碲化汞胶体量子点的迁移率和薄膜的掺杂状态进行测量。把碲化汞胶体量子点沉积在表面有一层薄SiO_2作为绝缘层的Si基底上,基底两侧的金电极分别作为漏极和源极,Si作为栅极,器件结构如图1(c)所示。通过控制栅极的极性和电压大小,可以使场效应晶体管分别处于截止或导通状态。图1(d)所示为N型、本征型和P型中波红外碲化汞胶体量子点的场效应晶体管转移曲线。利用FET传输曲线的斜率计算了载流子的迁移率μ_{FET},具体计算公式为

$$\mu_{FET}=\frac{L}{WC_iV_D}\cdot\frac{dI_D}{dV_g},\tag{1}$$

式中:$C_i=\frac{1}{\varepsilon_0\varepsilon_{sio_2}}\cdot\frac{1}{d}=11.5\times10^{-5}$ F/m,表示单位面积的电容(d=300 nm为SiO_2层的厚度);$L=10$ μm,表示叉指电极间的间距;$W=200$ μm×12,表示叉指电极的宽度;$V_D=1$ V,表示源极电压;$\frac{dI_D}{dV_g}$为转移曲线的斜率。经计算,短波、中波红外碲化汞胶体量子点载流子迁移率均超过1 $cm^2/(V\cdot s)$。

3　分析与讨论

3.1　碲化汞胶体量子点光电探测器的制备

光伏型探测器不需要施加额外的偏置电压,没有散粒噪声,理论上会具有更好的性能,借鉴文献[14]的研究结果,将器件结构设计为Al_2O_3/ITO/HgTe/Ag_2Te/Au,制备方法如下:

第一步,在蓝宝石基底上使用磁控溅射方法沉积50 nm ITO,ITO的功函数在4.5~4.7 eV范围内[43]。

第二步,制备约470 nm的本征型碲化汞胶体量子点薄膜。

第三步,取50 μL碲化银纳米晶体溶液滴在薄膜上,以3000 r/min转速旋转30 s。然后,将50 μL $HgCl_2/CH_3OH$(10 mmol/L)溶液滴在薄膜上静置10 s后,以3000 r/min转速旋转30 s,重复上述步骤两次。Ag^+作为P型掺杂层,与本征型碲化汞胶体量子点层形成P-I异质结。

第四步,将器件移至蒸发镀膜机中,在真空环境(5×10^{-4} Pa)下蒸镀50 nm Au作为顶层的电极。高迁移率光伏型探测器的结构和横截面扫描电子显微镜(SEM)图像如图2(a)所示,能级结构如图2(b)所示。所制备探测器的面积为0.2 mm×0.2 mm。

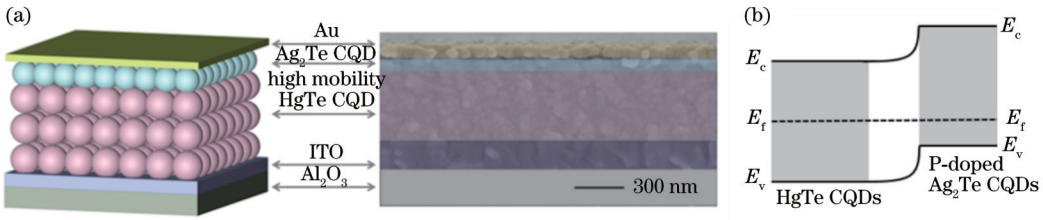

图2　器件结构设计。(a)高迁移率碲化汞胶体量子点P-I异质结结构示意图及SEM图像;(b)碲化汞胶体量子点P-I异质结能带结构

Fig. 2　Device structure design. (a) Structure schematic and cross-sectional SEM image of high mobility CQDs P-I heterojunction; (b) energy structure of CQDs P-I heterojunction

3.2　器件性能表征

为了探究高载流子迁移率短波红外和中波红外光伏型探测器的光电特性,测试了器件的I-V曲线以及响应光谱。图3(a)、(b)所示分别为高迁移率短波红外和中波红外器件的I-V特性曲线,可以看到,短波红外和中波红外探测器的开路电压分别为140 mV和80 mV,这表明P-I结中形成了较强的内建电场。此外,在零偏置电压下,高迁移率短波红外和中波红外器件的光电流分别为0.27 μA和5.5 μA。图3(d)、(e)分别为1.9~2.03 μm(300~80 K)的短波红外器件的响应光谱和3.5~4.2 μm(300~80 K)的中波红外器件的响应光谱。

比探测率D^*和响应度$\Re$是表征光电探测器性能的重要参数。$\Re$为探测器的响应度,用来描述器件的光电转换能力,即输出信号光电流与输入光信号功率之比,计算公式为

$$\Re=I_{ph}/P,\tag{2}$$

式中:I_{ph}为光电流,单位为A;P为输入光信号功率,单位为W。当黑体温度为874 K时,短波红外和中波红外器件的输入光信号功率分别为0.29 μW和5.46 μW。在零偏置电压下,短波红外和中波红外器件的$\Re$分别达到0.9 A/W(300 K)和1.0 A/W(80 K)。

D^*为探测器的比探测率,用来表征设备检测对象的能力,计算公式为

$$D^*=\frac{\Re}{N}\sqrt{A_d},\tag{3}$$

式中:N为噪声电流密度,单位为$A\cdot Hz^{-1/2}$;$\Re$为响应度,单位为A/W;A_d为探测器面积,单位为cm^2。

在零偏置电压下,实测噪声N与约翰逊噪声$N_{Johnson}$接近。约翰逊噪声的计算公式为

$$N_{Johnson}=\sqrt{4k_bT/R},\tag{4}$$

式中:k_b为玻尔兹曼常数,$k_b=1.38\times10^{-23}$ J/K;T为开尔文温度,单位为K;R为暗电流曲线上零偏置电压附

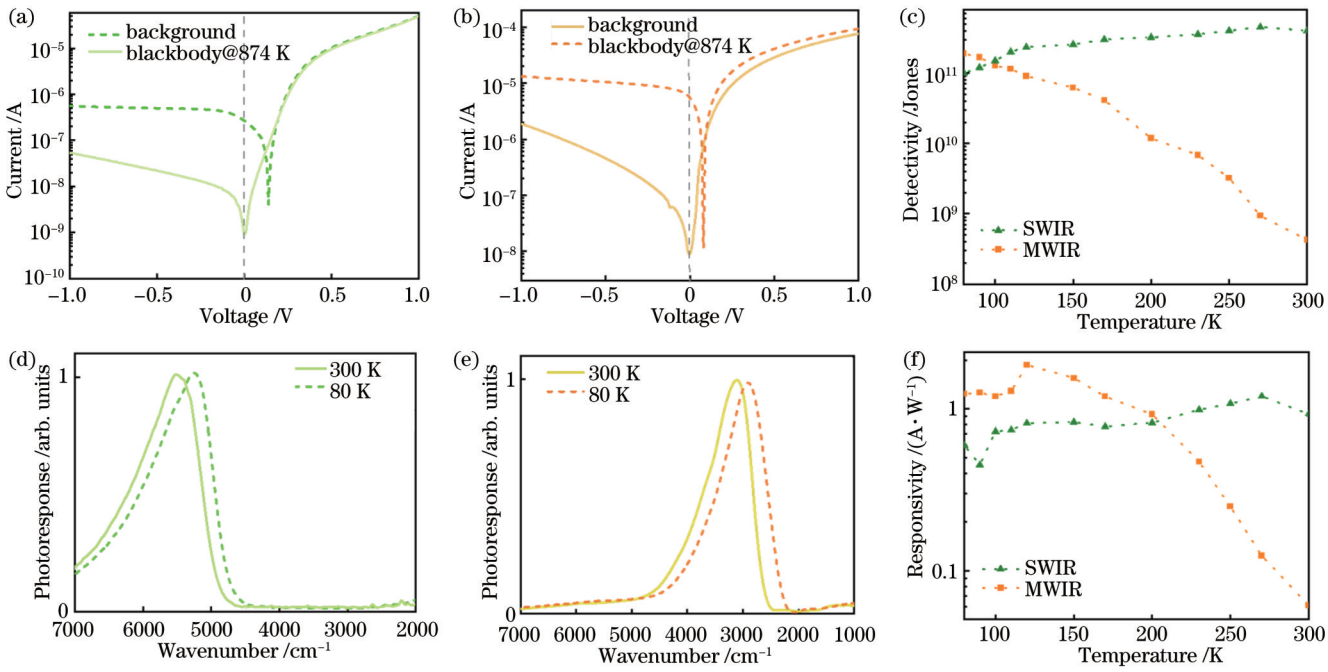

图 3 高载流子迁移率光电探测器性能。(a)300 K时短波红外 *I-V* 曲线；(b) 80 K时中波红外 *I-V* 曲线；(c)短波红外及中波红外器件的比探测率随温度的变化；(d)短波红外器件在80 K和300 K时的光谱响应；(e)中波红外器件在80 K和300 K时的光谱响应；(f)短波红外和中波红外器件的响应度随温度的变化

Fig. 3 Performance of the high carrier mobility photodetectors. (a) SWIR *I-V* curves at 300 K; (b) MWIR *I-V* curves at 80 K; (c) specific detectivity (D^*) as a function of the temperature of high mobility on SWIR and MWIR devices; (d) spectral response of SWIR device at 80 K and 300 K; (e) spectral response of MWIR device at 80 K and 300 K; (f) responsivity ($\Re$) as a function of the temperature of high mobility on SWIR and MWIR device

近拟合的电阻，短波红外和中波红外探测器的电阻分别为 7.7 MΩ和 416 kΩ。

图 3(c)、(f)给出了探测器的比探测率 D^* 和响应度 $\Re$ 随温度的变化。可以看到，短波红外器件在所有被测温度下，D^* 都可以达到 1×10^{11} Jones以上，中波红外器件在 110 K下的 D^* 达到了 1.2×10^{11} Jones。

根据响应度 $\Re$，也可以求出器件的外量子效率(η_{EQE})，计算公式为

$$\eta_{EQE}=1.24\Re/\lambda, \tag{5}$$

式中：λ 为器件的响应光谱对应的波长，单位为 μm。可以计算出 300 K下的短波红外器件的外量子效率达到 61%，110 K下的中波红外器件的外量子效率达到 30%。在之前的研究中，基于碲化汞胶体量子点的中波红外器件的外量子效率为 2%[17]或 17%[21]，短波红外器件的外量子效率为 50%[44]。外量子效率的提高是因为量子点本身迁移率的提高以及量子点的密集排列增强了光吸收。对于光伏型探测器，器件的总光电流来自电子-空穴对分离产生的光电流和扩散电流。当红外光入射到光敏层时，空间电荷区(SCR)产生的电子-空穴对会立即被异质结形成的内建电场分离，形成光电流。然而，在SCR外产生的电子对会扩散，其中一些会到达SCR并进行电荷分离，从而产生扩散电流。本征胶体量子点薄膜与匹配的掺杂层结合后，会产生更厚的SCR，而增强的内建电场有助于分离电子-空穴对。此外，碲化汞胶体量子点薄膜高迁移率的特性可以增加扩散载流子到达SCR并被收集的概率。

3.3 应用

本实验验证了高载流子迁移率的短波红外和中波红外量子点光电探测器的实际应用，如光谱仪和红外相机。光谱仪实验装置如图 4(a)所示，其内部主要是一个迈克耳孙干涉仪。图 4(b)、(c)所示为使用短波红外和中波红外量子点器件探测时有样品和没有样品的光谱响应结果。图 4(e)、(f)所示为样品在短波红外和中波红外波段的透过率曲线。对于短波红外波段，选择了 CBZ、DDT、BA 和 TCE 这 4 个样品，它们在可见光下都是透明的，肉眼无法进行区分，但它们的短波红外光谱响应和透过率不同。对于中波红外波段，选择了 PP 和 PVC 这两个样品，在可见光下它们都是白色的塑料，但它们的中波红外光谱响应和透过率不同。图 4(d)为自制短波红外和中波红外单点相机的扫描图像，其中短波相机扫描图像可以给出材质信息，中波红外相机扫描图像则反应热信息。例如，从烙铁的中波红外成像中可以清楚地了解烙铁内部的温度分布。在可见光下，硅片呈现不透明的状态；使用自制的短波红外相机成像后，硅片呈现半透明的状态。

4 结 论

采用混相配体交换的方法，将量子点薄膜中的载

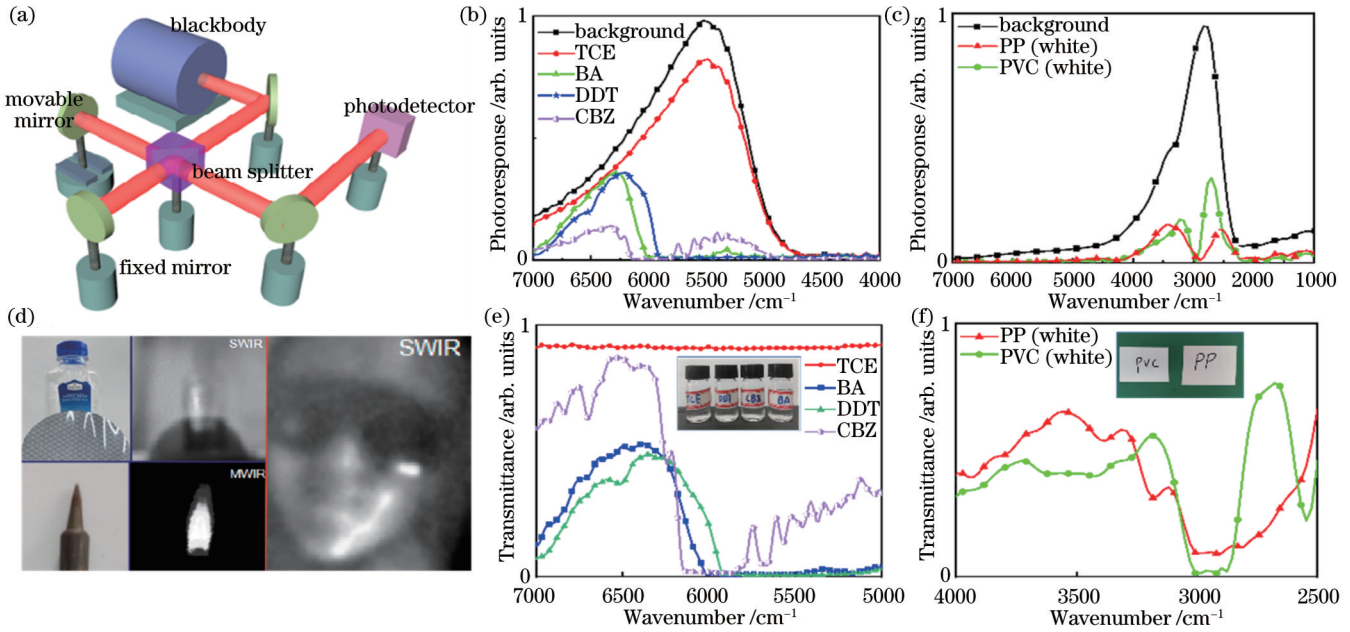

图 4 器件的应用。(a)利用高载流子迁移率探测器进行响应光谱测量的原理示意图；(b)(c)在有样品和没有样品两种模式下用自制探测器探测到的光谱响应；(d)自制短波红外和中波红外光电探测器的单像素扫描成像结果；(e) TCE、BA、DDT 和 CBZ 在短波红外模式下的透过率，插图为 4 个样品的可见光图像；(f) PVC 和 PP 在中波红外模式下的透过率，插图为 2 个样品的可见光图像

Fig. 4 Device application. (a) Experimental setup for absorption spectroscopy measurements with high-carrier mobility detectors; (b) (c) detector spectral responses with and without samples at SWIR and MWIR mode, respectively; (d) imaging result of SWIR and MWIR devices; (e) light transmittance of TCE, BA, DDT, and CBZ in SWIR mode, illustrations are the visible light images of four samples; (f) light transmittance of PVC and PP in MWIR mode, illustrations are the visible light images of two samples

流子迁移率提升到 1 $cm^2/(V\cdot s)$，相较于之前的研究结果提升了 2 个量级。通过加入汞盐实现了对量子点薄膜的掺杂调控，分别实现了 P 型、本征型以及 N 型的量子点薄膜。同时，基于本征型高迁移率量子点制备了短波红外和中波红外波段的光伏型光电探测器。测试结果表明，该探测器提升了量子点的输运性质，有效地提升了探测器的响应率、比探测率等核心性能，并成功运用于光谱仪和红外相机等。本研究结果可为低成本、高性能量子点红外光电探测器的发展提供参考。

参 考 文 献

[1] de Cumis M S, Viciani S, Borri S, et al. Widely-tunable mid-infrared fiber-coupled quartz-enhanced photoacoustic sensor for environmental monitoring[J]. Optics Express, 2014, 22(23): 28222-28231.

[2] 宋子壮, 杨嘉伟, 张东方, 等. 基于无监督域适应的低空海面红外目标检测[J]. 光学学报, 2022, 42(4): 0415001.
Song Z Z, Yang J W, Zhang D F, et al. Low-altitude sea surface infrared object detection based on unsupervised domain adaptation[J]. Acta Optica Sinica, 2022, 42(4): 0415001.

[3] 王虎, 罗建军, 白瑜. 空间非合作目标中波红外探测相机光学系统设计[J]. 光学学报, 2012, 32(s1): s122001.
Wang H, Luo J J, Bai Y. Optics system design of the middle-wave infrared camera for spatial non-cooperative targets[J]. Acta Optica Sinica, 2012, 32(s1): s122001.

[4] 谢家豪, 黄树彩, 韦道知, 等. 空天红外探测系统对无人机集群探测能力分析[J]. 光学学报, 2022, 42(18): 1812002.
Xie J H, Huang S C, Wei D Z, et al. Detectability analysis of air-space infrared detection system for UAV swarm[J]. Acta Optica Sinica, 2022, 42(18): 1812002.

[5] Madejová J. FTIR techniques in clay mineral studies[J]. Vibrational Spectroscopy, 2003, 31(1): 1-10.

[6] Rogalski A. Toward third generation HgCdTe infrared detectors [J]. Journal of Alloys and Compounds, 2004, 371(1/2): 53-57.

[7] Rogalski A, Antoszewski J, Faraone L. Third-generation infrared photodetector arrays[J]. Journal of Applied Physics, 2009, 105(9): 091101.

[8] González A, Fang Z J, Socarras Y, et al. Pedestrian detection at day/night time with visible and FIR cameras: a comparison[J]. Sensors, 2016, 16(6): 820.

[9] Velicu S, Grein C H, Emelie P Y, et al. MWIR and LWIR HgCdTe infrared detectors operated with reduced cooling requirements[J]. Journal of Electronic Materials, 2010, 39(7): 873-881.

[10] Cervera C, Baier N, Gravrand O, et al. Low-dark current p-on-n MCT detector in long and very long-wavelength infrared[J]. Proceedings of SPIE, 2015, 9451: 945129.

[11] Hoogeveen R W M, van der A R J, Goede A P H. Extended wavelength InGaAs infrared (1.0-2.4 μm) detector arrays on SCIAMACHY for space-based spectrometry of the Earth atmosphere[J]. Infrared Physics & Technology, 2001, 42(1): 1-16.

[12] Sarusi G. QWIP or other alternative for third generation infrared systems[J]. Infrared Physics & Technology, 2003, 44(5/6): 439-444.

[13] García de Arquer F P, Talapin D V, Klimov V I, et al. Semiconductor quantum dots: technological progress and future challenges[J]. Science, 2021, 373(6555): eaaz8541.

[14] Lu H P, Carroll G M, Neale N R, et al. Infrared quantum dots: progress, challenges, and opportunities[J]. ACS Nano, 2019, 13(2): 939-953.
[15] Keuleyan S, Lhuillier E, Brajuskovic V, et al. Mid-infrared HgTe colloidal quantum dot photodetectors[J]. Nature Photonics, 2011, 5(8): 489-493.
[16] Chen M L, Lan X Z, Tang X, et al. High carrier mobility in HgTe quantum dot solids improves mid-IR photodetectors[J]. ACS Photonics, 2019, 6(9): 2358-2365.
[17] Zhu B Q, Chen M Y, Zhu Q, et al. Integrated plasmonic infrared photodetector based on colloidal HgTe quantum dots[J]. Advanced Materials Technologies, 2019, 4(10): 1900354.
[18] Konstantatos G, Badioli M, Gaudreau L, et al. Hybrid graphene-quantum dot phototransistors with ultrahigh gain[J]. Nature Nanotechnology, 2012, 7(6): 363-368.
[19] Dong Y F, Chen M Y, Yiu W K, et al. Solution processed hybrid polymer: HgTe quantum dot phototransistor with high sensitivity and fast infrared response up to 2400 nm at room temperature[J]. Advanced Science, 2020, 7(12): 2000068.
[20] Guyot-Sionnest P, Roberts J A. Background limited mid-infrared photodetection with photovoltaic HgTe colloidal quantum dots[J]. Applied Physics Letters, 2015, 107(25): 253104.
[21] Ackerman M, Tang X, Guyot-Sionnest P. Fast and sensitive colloidal quantum dot mid-wave infrared photodetectors[J]. ACS Nano, 2018, 12(7): 7264-7271.
[22] Hafiz S B, Al Mahfuz M M, Lee S, et al. Midwavelength infrared p-n heterojunction diodes based on intraband colloidal quantum dots[J]. ACS Applied Materials & Interfaces, 2021, 13(41): 49043-49049.
[23] Jagtap A, Martinez B, Goubet N, et al. Design of a unipolar barrier for a nanocrystal-based short-wave infrared photodiode [J]. ACS Photonics, 2018, 5(11): 4569-4576.
[24] Rastogi P, Izquierdo E, Gréboval C, et al. Extended short-wave photodiode based on CdSe/HgTe/Ag_2Te stack with high internal efficiency[J]. The Journal of Physical Chemistry C, 2022, 126(32): 13720-13728.
[25] Martinez B, Ramade J, Livache C, et al. HgTe nanocrystal inks for extended short-wave infrared detection[J]. Advanced Optical Materials, 2019, 7(15): 1900348.
[26] Chen M L, Hao Q, Luo Y N, et al. Mid-infrared intraband photodetector via high carrier mobility HgSe colloidal quantum dots[J]. ACS Nano, 2022, 16(7): 11027-11035.
[27] Tang X, Ackerman M M, Chen M L, et al. Dual-band infrared imaging using stacked colloidal quantum dot photodiodes[J]. Nature Photonics, 2019, 13(4): 277-282.
[28] Gréboval C, Darson D, Parahyba V, et al. Photoconductive focal plane array based on HgTe quantum dots for fast and cost-effective short-wave infrared imaging[J]. Nanoscale, 2022, 14(26): 9359-9368.
[29] Zhang S, Bi C, Qin T L, et al. Wafer-scale fabrication of CMOS-compatible trapping-mode infrared imagers with colloidal quantum dots[J]. ACS Photonics, 2023, 10(3): 673-682.
[30] Wang C H, Cai J H, Ye Y Y, et al. Full-visible-spectrum perovskite quantum dots by anion exchange resin assisted synthesis[J]. Nanophotonics, 2022, 11(7): 1355-1366.
[31] Cai J H, Wang C H, Hu X P, et al. Water-driven photoluminescence reversibility in $CsPbBr_3$/PDMS-PUa composite[J]. Nano Research, 2022, 15(7): 6466-6476.
[32] Chen M L, Xue X M, Qin T L, et al. Universal homojunction design for colloidal quantum dot infrared photodetectors[J]. Advanced Materials Technologies, 2023, 8(16): 2300315.
[33] Kovalenko M V, Scheele M, Talapin D V. Colloidal nanocrystals with molecular metal chalcogenide surface ligands [J]. Science, 2009, 324(5933): 1417-1420.
[34] Tang J, Kemp K W, Hoogland S, et al. Colloidal-quantum-dot photovoltaics using atomic-ligand passivation[J]. Nature Materials, 2011, 10(10): 765-771.
[35] Nag A, Kovalenko M V, Lee J S, et al. Metal-free inorganic ligands for colloidal nanocrystals: S^{2-}, HS^-, Se^{2-}, HSe^-, Te^{2-}, HTe^-, TeS_3^{2-}, OH^-, and NH_2^- as surface ligands[J]. Journal of the American Chemical Society, 2011, 133(27): 10612-10620.
[36] Lan X Z, Chen M L, Hudson M H, et al. Quantum dot solids showing state-resolved band-like transport[J]. Nature Materials, 2020, 19(3): 323-329.
[37] Xue X M, Chen M L, Luo Y N, et al. High-operating-temperature mid-infrared photodetectors via quantum dot gradient homojunction[J]. Light: Science & Applications, 2023, 12: 2.
[38] Chen M L, Lan X Z, Hudson M H, et al. Magnetoresistance of high mobility HgTe quantum dot films with controlled charging [J]. Journal of Materials Chemistry C, 2022, 10(37): 13771-13777.
[39] Deng Z Y, Jeong K S, Guyot-Sionnest P. Colloidal quantum dots intraband photodetectors[J]. ACS Nano, 2014, 8(11): 11707-11714.
[40] Jeong K S, Deng Z Y, Keuleyan S, et al. Air-stable n-doped colloidal HgS quantum dots[J]. The Journal of Physical Chemistry Letters, 2014, 5(7): 1139-1143.
[41] Kroupa D M, Vörös M, Brawand N P, et al. Tuning colloidal quantum dot band edge positions through solution-phase surface chemistry modification[J]. Nature Communications, 2017, 8: 15257.
[42] Chen M L, Guyot-Sionnest P. Reversible electrochemistry of mercury chalcogenide colloidal quantum dot films[J]. ACS Nano, 2017, 11(4): 4165-4173.
[43] Park Y, Choong V, Gao Y, et al. Work function of indium tin oxide transparent conductor measured by photoelectron spectroscopy[J]. Applied Physics Letters, 1996, 68(19): 2699-2701.
[44] Ackerman M M, Chen M L, Guyot-Sionnest P. HgTe colloidal quantum dot photodiodes for extended short-wave infrared detection[J]. Applied Physics Letters, 2020, 116(8): 083502.

Infrared Detectors of High Carrier Mobility Colloidal Quantum Dots

Xue Xiaomeng[1], Ma Haifei[1,2], Hao Qun[1,2**], Tang Xin[1,2], Chen Menglu[1,2*]

[1]*School of Optics and Photonics, Beijing Institute of Technology, Beijing* 100081, *China*;

[2]*Yangtze Delta Region Academy of Beijing Institute of Technology, Jiaxing* 314019, *Zhejiang, China*

Abstract

Objective Short-wave infrared (SWIR) and mid-wave infrared (MWIR) bands catch much attention because of matching the atmosphere window. In this spectral range, solution-based zinc-blend HgTe colloidal quantum dots (CQDs) become a potential alternative to traditional epitaxial materials for photodetection. However, the performance of CQD photodetectors should be improved, and controlling the transport properties like doping and mobility would be the key to high-performance photodetectors. We employ the mixed phase ligand exchange method to achieve high carrier mobility in HgTe CQDs films, which is more than 1 $cm^2/(V\cdot s)$. Meanwhile, different doping types in HgTe CQD solid are realized, such as N, intrinsic, and P types. We also demonstrate that the high carrier mobility improves CQD photovoltaic performance. For example, SWIR and MWIR photovoltaic photodetectors are achieved with intrinsic high mobility HgTe CQDs solid, where the external quantum efficiency (EQE) is 61% for SWIR photovoltaic photodetectors and 30% for MWIR photovoltaic photodetectors. Additionally, the detectivity (D^*) is 4×10^{11} Jones at 300 K for SWIR photovoltaic photodetectors and 1.2×10^{11} Jones at 110 K for MWIR photovoltaic photodetectors.

Methods The mixed-phase ligand exchange process involves liquid-phase ligand exchange and solid-phase ligand exchange. In the liquid phase ligand exchange, 4 mL HgTe CQDs in n-hexane would mix with 160 μL β-ME and 8 mg DDAB in DMF, which is stewed for 10 s to accelerate separation. Then the solution is centrifuged, and after decanting the supernatant, 60 μL DMF is adopted to dissolve the CQD solids in centrifuge tubes to obtain stable CQD ink. In this method, β-ME replaces the long-chain ligand on the CQD surface in the liquid phase, and DDAB is a catalyst to assist CQDs transfer from n-hexane to the polar solvent DMF. The CQD films are prepared by spin or drop coating, and then solid-state ligand exchange with EDT/HCl/IPA (1∶1∶50 by volume) solution is performed for 10 s, rinsed with IPA, and dried with N_2. Solid-phase ligand exchange can both remove the additional hybrid ligands on the film surface and stabilize the Fermi level of CQD films. For controllable CQDs doping, as Hg^{2+} can stabilize electrons in CQDs by surface dipoles, we choose mercury salts such as $HgCl_2$ to regulate CQDs to intrinsic or N types, and in liquid phase ligand exchange, 10 mg $HgCl_2$ is added to obtain intrinsic CQDs, and 20 mg $HgCl_2$ is added to obtain N-type CQDs.

The photovoltaic photodetector structure is Al_2O_3/ITO/HgTe/Ag_2Te/Au. Fig. 2(a) shows the structure diagram and cross-sectional SEM of high-mobility photovoltaic photodetectors. In ambient conditions, a layer of about 50 nm ITO electrode is deposited on the Al_2O_3 substrate. The ITO serves as electron contact, and then a layer of HgTe CQDs film with high carrier mobility obtained by mixed ligand exchange is deposited by drop-coating. The CQDs film is an intrinsic type regulated by surface doping, which helps increase photocurrent. The HgTe CQDs surface is treated with EDT, HCl, and IPA (1∶1∶20 by volume), with the CQDs thickness of around 400 nm. The Ag_2Te nanoparticle solution (Ag^+ as P-doping) is prepared on the HgTe CQDs film by spin-coating. It is then exposed to 10 mmol/L $HgCl_2$/methanol solution, which is helpful to diffuse Ag^+ into the CQDs film. Finally, a layer of gold electrode is evaporated on top with 50 nm thickness. The energy diagram is shown in Fig. 2(b).

Results and Discussions Mixed-phase ligand exchange includes liquid-phase and solid-state ligand exchange, which can improve carrier mobility and control the doping density of HgTe CQDs by surface dipole regulation. The TEM image of the MWIR CQDs before and after the liquid phase ligand exchange is shown in Fig. 1(a). The spacing between CQDs is reduced with tight arrangement, which can improve the light absorption by HgTe CQDs and is conducive to improving device performance. Field effect transistor (FET) is adopted to measure the mobility and doping level of carriers in the film, and the structure is shown in Fig. 1(c). The FET transfer curves of N-type, intrinsic, and P-type MWIR HgTe CQDs are shown in Fig. 1(d). The slope of the FET transfer curve is utilized to calculate the carrier mobility. The carrier mobility of N-type, intrinsic type, and P-type SWIR and MWIR HgTe CQDs all exceeds 1 $cm^2/(V\cdot s)$. The *I-V* characteristic curves of high carrier mobility photovoltaic photodetectors on SWIR and MWIR are shown in Figs. 3(a) and (b), and the open circuit voltages on SWIR and MWIR photodetectors are 140 mV and 80 mV, which indicates a strong internal electric field. At zero bias, the photocurrents on high mobility SWIR and MWIR devices are 0.27 μA and 5.5 μA respectively. The input optical signal power of SWIR and MWIR at the blackbody temperature of 874 K is 0.29 μW and 5.46 μW respectively, and the responsivity ($\Re$) is obtained. At zero bias, $\Re$ reaches 0.9 A/W (at 300 K) and 1.0 A/W (at

80 K) for SWIR and MWIR devices respectively. The D^* of high carrier mobility SWIR photovoltaic photodetectors is 4×10^{11} Jones in all temperature ranges, and that of MWIR photovoltaic photodetectors is 1.2×10^{11} Jones at 110 K. Additionally, the EQE increases several-fold in high mobility photovoltaic photodetectors, where it is 61% for SWIR devices and 30% for MWIR devices.

Conclusions The carrier mobility in HgTe CQD films is increased to 1 $cm^2/(V\cdot s)$ by the mixed phase ligand exchange method. By adding salt, the doping control of P-type, intrinsic type, and N-type CQD films is realized. Meanwhile, photovoltaic photodetectors in SWIR and MWIR are prepared based on intrinsic high mobility CQD solid. For the 1.9 μm SWIR photodetectors, $\Re$ is 0.9 A/W and D^* is 4×10^{11} Jones at 300 K. For the 4.2 μm MWIR photodetectors, $\Re$ is 1.1 A/W and D^* is 1.2×10^{11} Jones at 110 K. In addition, the EQE would be improved to 61% for SWIR photodetectors at 300 K and 30% for MWIR at 110 K, without applied bias. The test results show that the transport property control of CQDs can improve the core performance of photodetectors, such as $\Re$ and D^*. Our study can promote the development of low-cost and high-performance CQDs infrared photodetectors.

Key words detectors; quantum dots; high mobility; photovoltaic infrared photodetectors; ligand exchange